PNAS RESEARCH ARTICLE | EARTH, ATMOSPHERIC, AND PLANETARY SCIENCES

Pulsed biogenic methane emissions coupled with episodic warming during the Toarcian Oceanic Anoxic Event

Ruoyuan Qiu[a,b], Zhichao Yu[a], Benjamin J. W. Mills[c], Renda Huang[d], Wang Zhang[a], Terry Isson[e], Bo Wan[f], Ruizhen Zhang[a,b], Mingyu Zhao[f,1], and Zhijun Jin[d,1]

Affiliations are included on p. 10.

Edited by Mark Thiemens, University of California San Diego, La Jolla, CA; received November 19, 2024; accepted July 23, 2025

Reconstructing carbon release fluxes during ancient climatic warming events is important for improving predictions of carbon cycle and climate dynamics under future anthropogenic warming scenarios. We investigate the extent of biogenic methane release and its contribution to climate variability across the Toarcian Oceanic Anoxic Event (T-OAE) approximately 183 million years ago. To do this, we developed a global biogeochemical model and applied a Bayesian inversion using Markov Chain Monte Carlo (MCMC) simulations. Based on a high-resolution record of carbon isotope excursions from the Yorkshire section, our results indicate that a release of at least 4,700 Gt carbon from biogenic CH_4 (with a carbon isotopic composition, $\delta^{13}C$ of −50 to −70‰) is necessary to accurately reproduce the pronounced pulsed shift in the $\delta^{13}C$, as well as the inferred changes in atmospheric pCO_2 and global temperature. This massive methane release may have led to a substantial increase in atmospheric pCH_4 and contributed to additional global surface warming, perhaps by more than 2 °C. We further elucidate that the liberation of methane may have been facilitated by an upsurge in methanogenesis alongside a concomitant decline in methane oxidation within organic-rich, sulfate-depleted marine environments. An active CH_4 cycle represents a positive feedback mechanism that exacerbates environmental deterioration during climatic warming events, ultimately contributing to mass extinction of marine life.

biogenic methane | Toarcian Oceanic Anoxic Event | Bayesian inversion | carbon cycle perturbation | extreme warming

Significance

Large-scale release of biogenic methane has the potential to contribute to significant climate change, yet its role during hyperthermal events remains debated. Our results demonstrate that biogenic methane release played a pivotal role during the Toarcian Oceanic Anoxic Event (T-OAE). Episodic pulses of biogenic methane drove abrupt spikes in atmospheric methane concentrations and surface temperature increases of approximately 2 °C. These findings highlight the potential for methane feedback loops to exacerbate climate change, offering critical insights for predicting the dynamics of anthropogenic warming.

The Early Jurassic Toarcian Oceanic Anoxic Event (T-OAE, ~183 Ma) represents one of the most severe carbon cycle perturbations in the Mesozoic era (1). There was a rapid several-fold increase in atmospheric CO_2 concentrations (perhaps from ~250 to 1,000 ppm) over a short time interval of less than 0.5 million years (2). This transition from the Late Pliensbachian to the Early Toarcian was accompanied by a surface temperature rise of at least 6 °C at high latitude, as recorded in the stable oxygen isotope composition of belemnite (3). This climate shift led to widespread marine anoxic conditions (4), resulting in the deposition of laminated black shales in marine sediments with high organic carbon content (5). The rapidly warming (6), low-oxygen (4), and likely acidifying (7) ocean conditions triggered two distinct extinction pulses—first eliminating 67%, then an additional 50% of marine invertebrate species (both benthic and planktonic)—during two rapid negative carbon isotope excursions (8, 9).

The T-OAE is characterized by pronounced, high-amplitude, stepwise, and pulsed decreases in $\delta^{13}C$ values of global marine and terrestrial archives—both organic and inorganic—culminating in a total magnitude exceeding 6‰ (10, 11), forming one of the most extreme negative carbon isotope changes in the geological record and typically displaying a three-phase pattern: falling limb, plateau, and rising limb (10). Although high-precision zircon U-Pb ages from volcanic tuffs in the Sakuraguchi-dani section of Japan (12) and the Chacay Melehue section of Argentina (13) constrain the timing of the T-OAE, the exact duration of the associated $\delta^{13}C$ excursion remains uncertain. Nonetheless, the estimated duration of 200 to 300 ky is considered reasonable, as it encompasses a ~100 ky rising limb of the $\delta^{13}C$ excursion, which is consistent with the *e*-folding timescale for full carbon removal in carbon cycle models (14). Moreover, the durations of both the rising limb and the entire event are comparable to those of the Paleocene–Eocene Thermal Maximum (PETM) (15). The global records during the falling limb phase of the T-OAE show multiple high-frequency, pulsed negative $\delta^{13}C$ shifts, which are consistently observed across marine carbonate (16), marine organic matter (17), and terrestrial organic matter records (18, 19) (Fig. 1), indicating significant short-term perturbations in the carbon cycle (20). Although this typical pattern reflects linkages between episodic carbon releases,

Author contributions: R.Q., M.Z., and Z.J. designed research; R.Q. and M.Z. performed research; R.Q., R.H., W.Z.,and M.Z. contributed new reagents/analytic tools; R.Q., B.W., R.Z., and Z.Y. analyzed data; and R.Q., B.J.W.M., T.I., and M.Z. wrote the paper.

The authors declare no competing interest.

This article is a PNAS Direct Submission.

[1]To whom correspondence may be addressed. Email: mingyu.zhao@mail.iggcas.ac.cn or jinzj1957@pku.edu.cn.

This article contains supporting information online at https://www.pnas.org/lookup/suppl/doi:10.1073/pnas.2423598122/-/DCSupplemental.

Published September 2, 2025.

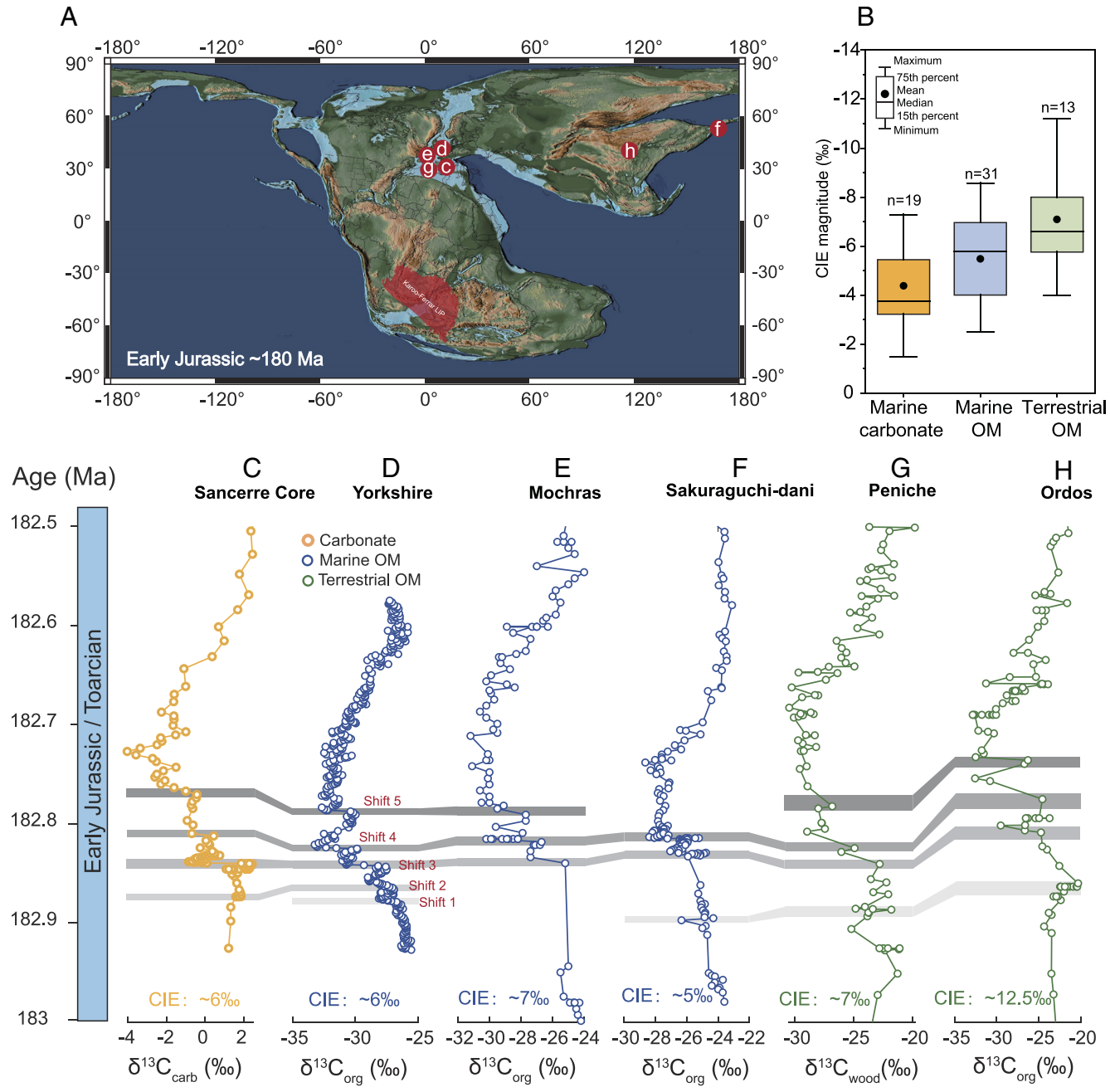

Fig. 1. Comparison of representative marine and terrestrial carbon isotope records in various depositional settings during the Toarcian-OAE. (*A*) Paleogeographic reconstruction of the Early Jurassic (180 Ma), with red dots marking locations of representative CIE records associated with the T-OAE. (*B*) Boxplot showing the magnitudes of CIEs across three substrates: marine carbonates, marine organic matter (OM), and terrestrial OM, compiled from literature data. "n" indicates the number of $\delta^{13}C$ records included. (*C*) Marine carbonate $\delta^{13}C$ record from the Sancerre Core borehole (France) (16). (*D*) The marine organic $\delta^{13}C$ records from the Yorkshire section (UK) (9). (*E*) Marine organic $\delta^{13}C$ records from the Mochras drilling (Wales) (17). (*F*) Marine organic $\delta^{13}C$ records from the Sakuraguchi-dani succession (Japan) (12). (*G*) $\delta^{13}C$ records of terrestrial organic matter (phytoclast separates) in the Peniche section (Portugal) (18). (*H*) Terrestrial organic $\delta^{13}C$ records from the Ordos Basin (China) (19). These marine and terrestrial records collectively reveal that pulsed negative shifts along the falling limb of the CIE are a globally consistent feature.

pulsed $\delta^{13}C$ fluctuations, and the climate responses, the sources and mechanisms of carbon release remain unclear.

A fundamental debate centers on whether a massive release of biogenic methane is necessary to explain the pulsed $\delta^{13}C$ shifts during the Toarcian. Proponents argue that methane produced by microbes has very low $\delta^{13}C$ values (~−50 to −70‰), meaning that even a relatively small release could significantly affect the $\delta^{13}C$ signatures (9, 11). Some have raised concerns that the rapid and sustained release of biogenic methane is difficult to detect, due to ambiguous storage and release mechanisms (21, 22). Similar debates persist for the PETM, where both the hypothesized role of massive biogenic methane release and the uncertainties surrounding its source and rate have been extensively discussed (23–25). Model simulations suggest that the activity of the Karoo-Ferrar Large Igneous Province (K-F LIP), which coinciding with the T-OAE (26), could account for the magnitude of the CIE through volcanic degassing and the release of thermogenic carbon generated by the heating of Permian coal seams in the Karoo Basin by intrusive magmatism (27), without requiring the release of biogenic methane (21). However, this volcanism-based

mechanism lacks robust evidence to fully support such rapid and large-magnitude $\delta^{13}C$ shifts. In particular, previous simulations have failed to reproduce the precise sharp and pulsed nature of the observed $\delta^{13}C$ shifts, leaving the role of biogenic methane during the T-OAE as a key unresolved question.

To address this issue, we developed a global biogeochemical model with oceanic and atmospheric methane dynamics (*Materials and Methods*). We selected three key paleoenvironmental metrics—$\delta^{13}C$ of organic carbon, pCO_2, and global sea surface temperature—and employed Markov Chain Monte Carlo (MCMC) approach on a High-Performance Computing (HPC) platform to perform Bayesian inversion, estimating the most likely rates and isotopic compositions of CH_4 and CO_2 injections during the T-OAE (*SI Appendix*, Fig. S1). Our results indicate that a substantial release of at least 4,700 Gt C from biogenic methane is necessary to account for the rapid, pulsed CIEs during the Toarcian carbon perturbations.

An Inversion Biogeochemical Model With Atmosphere Methane Cycle

In this study, we expanded upon the global biogeochemical model described in ref. 28 by incorporating both the oceanic and atmospheric methane cycles. This extension enabled us to investigate the relationship between pulsed negative $\delta^{13}C$ excursions and methane cycling. This model, named the CHemical Evolution of Earth Surface spheres (CHEES) (*SI Appendix*, Fig. S1 and Tables S1–S3), tracks the global cycles of organic and inorganic carbon, sulfate, sulfide, Fe, O_2, P, and CH_4 in a five-box ocean and one-box atmosphere system. Specifically, this model considers methane oxidation in the water column, methane oxidation in the atmosphere by OH radicals, and the climate effects of escaping methane. Using a nonlinear model to depict the methane oxidation process under varying atmospheric oxygen levels (29), we calibrated the methane oxidation coefficient (*km*) by reproducing the residence time of methane in the modern system (*Materials and Methods*). Additionally, we employed a one-dimensional photochemical and radiative climate model to obtain the relationship between global mean temperature and methane concentration (*SI Appendix*, Text 1). The resulting pCH_4-T relationship was incorporated into our model to simulate the climatic effects of methane (*Materials and Methods* and *SI Appendix*, Fig. S3 and Table S4).

We solve for three unknowns (CO_2 release, CH_4 release, and $\delta^{13}C$ of the released CH_4) through model–data comparisons with three independently constrained environmental metrics ($\delta^{13}C$, pCO_2, temperature). Carbonate records are susceptible to alteration due to dissolution and reprecipitation during diagenesis (30). Moreover, the resolution of current bulk carbonate records may be limited by biological disturbances (31), potentially obscuring the original signals. In contrast, organic carbon in laminated black shales—owing to minimal bioturbation—may retain high-resolution $\delta^{13}C$ signals (32), although potential biases arising from environmental controls on carbon isotope fractionation should be considered. On this basis, we selected the $\delta^{13}C$ record from the well-preserved, laminated, organic-rich black mudstones in Yorkshire, UK, as the target curve for the simulation, as it represents one of the most complete stratigraphic records globally, capturing multiple pulsed global CIEs (9). These multiple pulsed CIEs, observed in both marine and terrestrial sediments across geographically distinct regions (Fig. 1), carry global significance (18, 20). The target CIE magnitude in Yorkshire (−5 to −7‰) falls within the range of marine organic carbon $\delta^{13}C$ records (25th percentile CIE: −4.0‰; 75th percentile CIE: −6.9‰; average CIE: −5.7‰; n = 31), and partially overlaps with the range of carbonate $\delta^{13}C$ records (25th percentile CIE: −3.7‰; 75th percentile CIE: −5.3‰; average CIE: −4.3‰; n = 19). This indicates that the selected target likely faithfully records the magnitude of the CIE shift in external carbon reservoir (Fig. 1*B*), although pCO_2-driven changes in carbon isotope fractionation during photosynthesis may still have contributed to the signal. Additionally, we used published high-resolution pCO_2 reconstructions (2), derived from the C_3 plant proxy *Brachyoxylon* in the Tethys region (33). This method relies on a well-established relationship between atmospheric pCO_2 and photosynthetic carbon isotope discrimination ($\Delta^{13}C$), which increases with rising pCO_2 under non-stressed conditions (34). The proxy material was from subtropical coastal environments with ample water availability (35, 36), minimizing the influence of water stress on stomatal behavior and isotopic fractionation, thereby supporting the reliability of the reconstructed pCO_2 values (37). Finally, we applied oxygen isotope data from invertebrate fossils (3), corrected for latitudinal temperature effects (38), to derive the global average temperature, which served as the third inversion constraint. The timescale of T-OAE is based on the *tenuicostatum–serpentinum* zonal boundary age (~183.22 ± 0.25 Ma) from the Neuquén Basin in Argentina (13), along with the initiation (~182.906 ± 0.072 Ma) and termination (~182.489 ± 0.055 Ma) ages of the T-OAE, as determined by U–Pb zircon dating of volcanic tuffs (12). This set of zircon-based ages supports a robust duration of ~200 to 300 ky for the T-OAE. To capture the rapid oscillations in the $\delta^{13}C$ record while accounting for uncertainties in the estimated pCO_2 and temperature, we prioritized the carbon isotope component in error assessment when calculating the total log-likelihood, while errors contributed from pCO_2 and temperature were only considered if their simulated values fall outside the observed range (*Materials and Methods*).

We developed a time-sequential progression approach based on the MCMC method (39) to externally execute the integrated CHEES model for Bayesian inversion (*Materials and Methods*). Once the initial input parameters φ_0 (CO_2 release, CH_4 release, and $\delta^{13}C$ of the released CH_4) are provided and the model begins running, it continuously iterates under the joint control of six modules of the inversion framework until the MCMC algorithm completes its final iteration (*SI Appendix*, Fig. S1). Once the model reached convergence, as indicated by the close agreement between simulated outputs and observational constraints on $\delta^{13}C$, pCO_2, and temperature (*Materials and Methods*), we recorded the resulting ranges of output variables, including $\delta^{13}C_{POC}$, temperature, pCO_2, and pCH_4. The inverse model allows us to derive the amounts of CH_4 and CO_2 release, along with the isotopic composition of injected CH_4 (*Materials and Methods*). Each scenario underwent 1,000 independent MCMC runs to identify the input conditions that most closely reproduce the proxy data (*SI Appendix*, Table S6). Fig. 2 shows the average output from these CHEES model runs of Scenario 1 compared with the $\delta^{13}C_{POC}$, temperature, and pCO_2 records. The full model outline and code are included in *SI Appendix*.

Substantial Injections of Biogenic Methane During the T-OAE

Our model results indicate that only a carbon source with $\delta^{13}C$ values from −50 to −70‰—interpreted as biogenic methane—can accurately reproduce the high-frequency CIEs observed during the T-OAE, while also matching the pCO_2 and temperature trends (Fig. 2 and *SI Appendix*, Figs. S4 and S5 and Table S7). Specifically, the model successfully reproduces the five pulsed negative

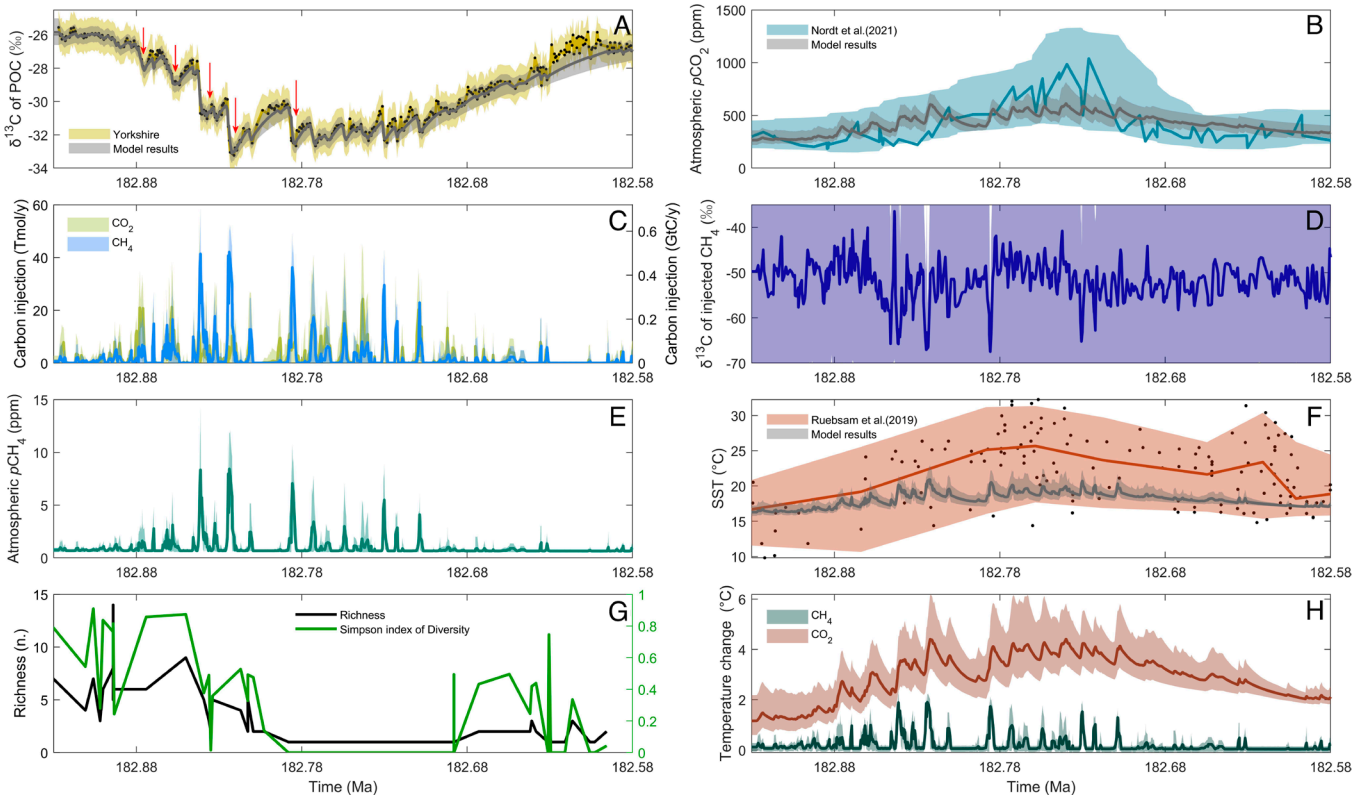

Fig. 2. Paleoenvironmental data and model outputs for Scenario 1. Model outputs represent results from 1,000 postconvergence runs of the MCMC algorithm. This simulation incorporates potential temporal variations in methane $\delta^{13}C$ to investigate global changes in methane isotopes, assuming CO_2 isotope values range from −5 to −25‰. Associated 95% credible intervals are shown as shaded areas, with the median values indicated by solid lines. (*A*) Observed $\delta^{13}C_{org}$ of particulate organic carbon (POC) from the Yorkshire (UK) section (9), and corresponding model outputs. The red arrows indicate five pulsed negative $\delta^{13}C$ excursions. (*B*) Reconstructed atmospheric pCO_2 from wood-based C_3 plants photosynthetic discrimination (2) and model outputs. (*C*) Model results for CO_2 and CH_4 emissions. Red numbers mark five pulses of CH_4 emission. (*D*) Modeled $\delta^{13}C$ value of the injected CH_4. (*E*) Atmospheric CH_4 concentration. (*F*) Global average surface temperature (GAST) reconstruction based on the $\delta^{18}O$ of belemnites (3), along with model outputs. The black dots represent the oxygen isotope records of belemnites. (*G*) Raw species richness (black) and Simpson's diversity index (green) of benthic faunas, including bivalves and brachiopods (40). Raw species richness reflects the number of distinct taxa in a given region or sample. Simpson's index ranges from zero to one, with lower values indicating dominance by a single taxon, and values closer to one suggesting even distribution among taxa. (*H*) Isolated temperature changes driven by CO_2 and CH_4, respectively.

excursions of 1 to 3‰ during the falling limb and plateau phases of the T-OAE, capturing the onset and duration of each pulse (based on the time scale for the Yorkshire section, projected from U–Pb zircon ages): first pulse (182.878 to 182.877 Ma); second pulse (182.862 to 182.857 Ma); third pulse (182.843 to 182.837 Ma); fourth pulse (182.825 to 182.823 Ma); fifth pulse (182.791 to 182.785 Ma), as well as the recovery in $\delta^{13}C$ between pulses (Fig. 2). Moreover, the model successfully reproduces the $\delta^{13}C$ recovery phase following the final negative shift, with a duration consistent with model-based carbon cycle responses to major perturbations. Initially, we performed three simulations to invert for the carbon isotopic composition of released methane ($\delta^{13}C_{CH4}$) (Scenarios 1 to 3), in which $\delta^{13}C_{CH4}$ was allowed to adjust dynamically over time within a broader range of −30 to −70‰. In Scenario 1, $\delta^{13}C_{CO2}$ fluctuated randomly from −5 to −25‰; in Scenario 2, $\delta^{13}C_{CO2}$ was fixed at −25‰; and in Scenario 3, $\delta^{13}C_{CO2}$ was fixed at −5‰ (*SI Appendix*, Table S7). The three inversion results reveal that $\delta^{13}C_{CH4}$ consistently remained below −50‰ during the T-OAE, with the minimum value reaching −70‰ (Fig. 2*D* and *SI Appendix*, Figs. S4*D* and S5*D*). Notably, these results are independent of the assumed $\delta^{13}C$ value of CO_2 input ($\delta^{13}C_{CO2}$ in the range of −5 to −25‰). Even when $\delta^{13}C_{CO2}$ is fixed at −25‰ (i.e., all CO_2 is sourced from the oxidation of organic matter), $\delta^{13}C_{CH4}$ values still remain below −50‰ throughout the T-OAE (*SI Appendix*, Figs. S4*D* and S5*D*). These findings provide robust support for biogenic methane emissions during the T-OAE.

If methane were entirely generated by the thermal cracking of coal beds (with $\delta^{13}C_{CH4}$ in the range of −30 to −40‰ and $\delta^{13}C_{CO2}$ in the range of −5 to −25‰, Scenario 4), achieving a total negative CIE of ~6‰ would require a much greater release of methane compared to biogenic sources, leading to pCO_2 levels far exceeding proxy estimates (*SI Appendix*, Fig. S6*B*). Importantly, this scenario fails to reproduce the five pulsed negative $\delta^{13}C$ shifts (*SI Appendix*, Fig. S6*A*). Although the possibility of mixed methane emissions, including those from thermal alteration of coal (41), remains plausible, our findings strongly indicate that biogenic methane contributed substantially to the carbon cycle and climate perturbations during the T-OAE, with subsea methane likely being one of its primary sources—a view closely aligned with interpretations of the PETM (23, 24, 42).

Sensitivity analyses under a range of parameter configurations (*SI Appendix* and *Materials and Methods*) demonstrate that reproducing the full magnitude and duration of the T-OAE $\delta^{13}C$ excursion requires a cumulative release of approximately 17,000 to 73,000 Gt of carbon over 200 ky (*SI Appendix*, Text 5). As our model simulations indicate, in each of these five pulsed carbon release events, ~200 to ~1,100 Gt of carbon was very rapidly released within about 2,000 years (Fig. 2). Notably, a single pulse releases more carbon than the total anthropogenic emissions since the Industrial Revolution (~400 Gt C), and the cumulative release across all five pulses (≥4499 Gt C) is comparable to the estimated total modern reserves of oil and natural gas (<5,000 Gt C) (43). The scale and tempo of these carbon pulses exceed the capacity of

steady-state natural carbon cycling, suggesting that episodic mobilization of long-term geological reservoirs may have played a critical role. Indeed, simulations that incorporate a marine methane capacitor (which will be discussed in the next section) further indicate that at least ~5,200 Gt of carbon from biogenic methane is required to match the observed $\delta^{13}C$ shifts (Fig. 4 and *SI Appendix*, Text 5 and Table S7 and Fig. S19). When the model includes a CO_2-dependent fractionation during photosynthesis (*SI Appendix*, Text 6 and Figs. S24 and S25), the lower bound is moderately reduced, with a minimum requirement of ~4,700 Gt of carbon from biogenic methane (*SI Appendix*, Fig. S26).

The estimated total carbon release (17,000 to 73,000 Gt of carbon) contrasts with previous estimates based on carbon isotope mass-balance calculations (1,500 to 2,700 Gt C) (11) and box model studies assuming low climate sensitivity and predefined carbon sources (15,340 to 24,750 Gt C) (21, 22). A key contributing factor is that our model precisely replicates the pulsed CIEs, including the five major ones. Reproducing these rapid pulses, particularly those during the falling limb, necessitates a greater carbon release than to match only the longer-term trend. Our findings also support the observation that the Mesozoic climate system exhibited greater sensitivity to CO_2 forcing than the present climate (44), with optimal model performance (maximum logarithmic likelihood) achieved at climate sensitivity values of 4 to 6 °C (*SI Appendix*, Fig. S8*A*). This elevated climate sensitivity likely has amplified chemical weathering through greater increases in temperature (45), thereby necessitating proportionally greater carbon emissions to achieve climatic equilibrium (*SI Appendix*, Fig. S8*G*). Although variations in the carbon budget required for system equilibrium—such as changes in background carbonate degassing flux—can influence the inferred carbon injection fluxes, our simulations adopted a lower-end degassing flux, resulting in the most conservative estimates (*SI Appendix*, Figs. S8 *C, F,* and *I*). Additionally, the assumed $\delta^{13}C$ values of CH_4 and CO_2 were found to play a decisive role in determining the model outcomes. Specifically, as the $\delta^{13}C$ of released CH_4 becomes more negative, the model better reproduces the negative $\delta^{13}C_{POC}$ values and the pulsed structure, reducing the required emissions of CH_4 and CO_2 (*SI Appendix*, Fig. S8). Likewise, a more negative $\delta^{13}C_{CO2}$ reduces the required methane release; for instance, fixing $\delta^{13}C_{CO2}$ at −25‰ instead of −5‰ necessitates approximately 10,000 Gt less C release from methane on average (*SI Appendix*, Table S7). Crucially, while these parameter variations determine the amount of CH_4 and CO_2 released, they do not change the central conclusion that biogenic methane was a key source of carbon release during the T-OAE.

The Source of Biogenic Methane

Of the ~10 Tmol y^{-1} of natural methane emissions to the atmosphere today, ~8.7 Tmol y^{-1} originates from terrestrial sources (46), while only ~1.3 Tmol y^{-1} derives from marine environments (47). This disparity is largely due to efficient anaerobic oxidation of methane (AOM) in sediments and oxidation in the water column, which together act as major barriers preventing most marine methane from reaching the atmosphere (48). A key difference between modern oceans and those of the Early Jurassic lies in seawater sulfate concentrations [modern: ~28 mM VS. Early Jurassic: ~12 mM] (49, 50), which likely limited the efficiency of AOM in the past, allowing more methane to escape from marine sediments to the atmosphere. To quantify how this reduced sulfate availability during the Early Jurassic modulated the background methane release from marine settings, we applied a one-dimensional reactive transport diagenetic model, SEDCHEM (51, 52). The results suggest that the background methane emissions from marine sources during the Early Toarcian were approximately 5.95 Tmol y^{-1}, about 4.6 times the modern level (*SI Appendix*, Text 4 and Table S10). This remains conservative as it does not account for reduced methane oxidation efficiency caused by lower pO_2 levels and diminished marine dissolved oxygen concentrations during the Early Jurassic.

In the modern ocean, methane seepage fluxes at sulfate-methane transition zones (SMTs) are predominantly governed by organic carbon flux (53). To illustrate variations in organic carbon flux that can be converted into CH_4 by methanogens in anoxic environments during the T-OAE, we quantified variations in TOC and organic carbon burial fluxes across six continental margin seas (0 to 2,000 m depths; *SI Appendix*, Table S9 and Fig. S15). In this calculation, we used the Dynamic Time Warping (DTW) algorithm (54–57) to align global marine sections with the timescale established by high-precision zircon CA-ID-TIMS U-Pb geochronology (12) (detailed DTW procedures can be found in *SI Appendix*, Text 2 and Table S8 and Figs. S9–S14). Results show that TOC and organic carbon accumulation rates (OCAR) increased across all six continental margin regions, with a substantial increase in global organic carbon burial during the T-OAE (*SI Appendix*, Fig. S16). The observed increase in global organic carbon burial is consistent with predictions from the CHEES model (*SI Appendix*, Fig. S17). Although the limited data points may slightly overestimate the magnitude of this change, the findings nevertheless point to a rise in organic carbon flux available for benthic microbial methanogenesis.

The outputs from the CHEES model, under the assumption that all CH_4 originates from biogenic sources, indicate that the average methane flux during the T-OAE increased by approximately 6.59 Tmol y^{-1} (5.81 to 7.21 Tmol y^{-1} in Scenarios 1 to 4) relative to pre-T-OAE levels (*SI Appendix*, Table S7). We used the SEDCHEM model to determine whether enhanced benthic microbial methanogenesis in the ocean sediments during the T-OAE could account for the increased biogenic methane injection indicated by the CHEES model (*SI Appendix*, Text 4). The organic matter loading fluxes and seawater sulfate levels across the T-OAE in the SEDCHEM model were derived from CHEES outputs. The results demonstrate a ~20 to 68% increase in benthic methanogenesis during the T-OAE, which translates to a ~1.19 to 4.05 Tmol y^{-1} rise in total methane emission from the ocean (Fig. 3).

The generated methane would be partially sequestered within the marine methane capacitor system, which exhibits potential instability under warming conditions and may undergo rapid release within a relatively short geological time interval (23). This pattern demonstrates striking parallels with the PETM (24), suggesting the presence of a significant dynamic methane capacitor system during the T-OAE that played a crucial regulatory role in the exogenic carbon cycle. To quantitatively assess the impact of this dynamic methane capacitor system on model outputs, we integrated this benthic methane reservoir into the CHEES model, establishing a robust linkage with the exogenic carbon cycle (*SI Appendix*, Text 5). The simulation outcomes successfully reproduced high-frequency CIEs and corresponding trends in pCO_2 and global temperature (*SI Appendix*, Fig. S19). When carbon isotope fractionation during photosynthesis is taken into account, the model requires a minimum of ~4,700 Gt of methane-derived carbon to reproduce the observed high-frequency $\delta^{13}C$ shifts. Sensitivity analysis further reveals that as the proportion of methane originating from marine methane capacitor systems increases, the total methane emissions required to reproduce the CIE decrease (Fig. 4). This is because

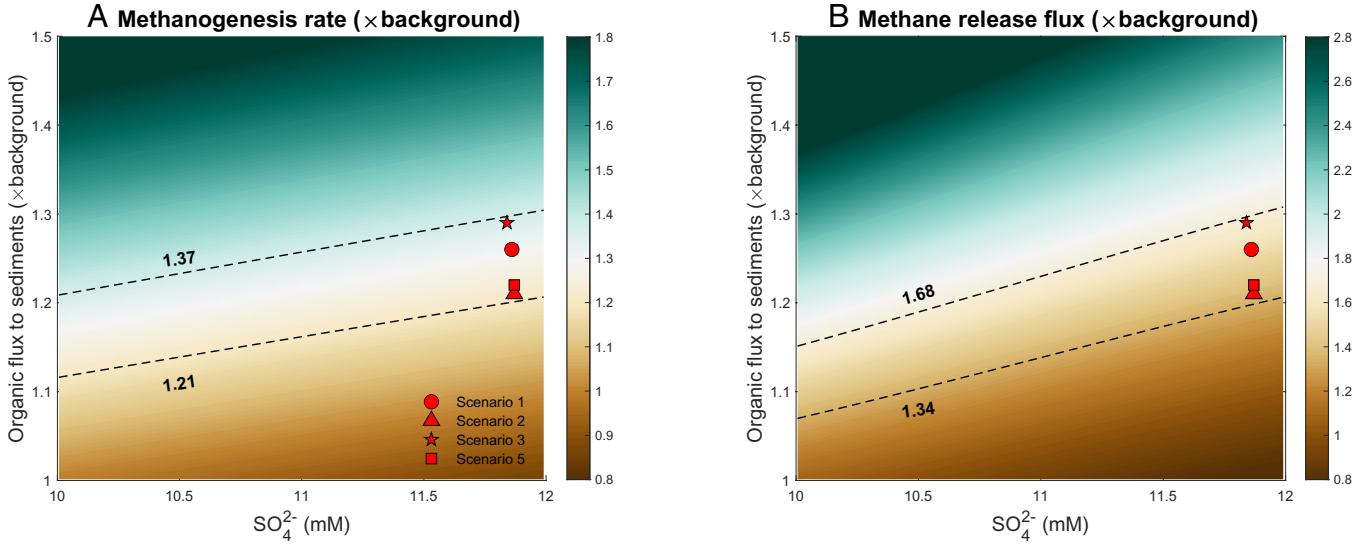

Fig. 3. Marine microbial methanogenesis rates during the T-OAE, as simulated by the SEDCHEM model. (*A*) Methanogenesis rates and (*B*) methane release fluxes from sediments to seawater under varying sulfate concentration (SO_4^{2-}) and organic matter flux to sediments. Methanogenesis rates, methane fluxes from sediments to seawater, and organic matter fluxes to sediments are all scaled relative to their respective background values prior to the T-OAE. The background value for seawater sulfate concentration prior to the T-OAE was set as 12 mM (49, 50). The red markers represent four successful simulations, assuming all methane originated from biogenic sources, which accurately reproduced the climate conditions during the T-OAE. The black dashed lines represent the upper and lower bounds of benthic microbial methanogenesis in these successful simulations. The color gradient reflects variations in the model outputs, with greener shades indicating higher values. More details on the parameters and boundary conditions for running the SEDCHEM model are provided in *SI Appendix*, Text 4 and Table S10.

a portion of the released methane undergoes oxidation in the water column, which has a more direct influence on DIC and its isotopic composition.

Beyond biogenic methane from the ocean, methane-induced warming likely amplified climatic feedbacks via permafrost thawing (releasing additional methane) (3), enhanced phosphorus weathering (45), and elevated methane production in terrestrial paleolakes and wetlands (58), collectively establishing a coupled framework for anomalous methane emissions during the T-OAE. Notably, modern lakes—particularly in boreal or temperate settings—can emit methane rapidly through ebullition, thereby bypassing oxidation in the water column (59). A similar feedback has been observed during Dansgaard–Oeschger events in the last glacial period, when abrupt warming was accompanied by rapid increases in atmospheric methane, likely driven in part by terrestrial sources such as wetlands and lakes (60, 61). Compared to more slowly responding marine systems, lakes, and wetlands—if widespread during the T-OAE—could have rapidly amplified the initial warming by releasing large amounts of methane.

The Effects of Methane Release on Climate and the Mass Extinction

The warming effect induced by K-F LIP activity likely served as the principal driver of methane release from terrestrial peatlands, permafrost, and marine capacitor system (62, 63). The transient yet potent radiative forcing of methane suggests that its rapid increase in the short term could precipitate abrupt transient temperature spikes (62), thereby exacerbating the warming effect and establishing a positive feedback loop that facilitates additional methane release. The pulsed release of methane was significantly controlled by precession cycles (*SI Appendix*, Figs. S21 and S22), indicating that orbital-driven warming played a crucial role in driving methane emissions (9). We simulated a total warming of ~6 °C during the Toarcian. Each rapid negative $\delta^{13}C$ excursion corresponded to a geologically rapid temperature increase, notably during the five negative excursions between 182.883 and 182.784 Ma (pulses 1 to 5), where $\delta^{13}C$ values dropped by 1 to 3‰ each time, with the pulses 3 (~182.842 Ma) and 4 (~182.822 Ma) directly contributing to a ~2 °C global temperature rise within 2,000 years. (Fig. 2 and *SI Appendix*, Figs. S4*H*, S5*H*, and S7*H*).

These consecutive warming events led to successive waves of extinction, with the third and fourth negative excursions corresponding to rapid decreases in marine biodiversity—an initial abrupt decline of 67%, followed by an additional loss of 50% of marine invertebrate species (8). As a result, for approximately 100 ky between 182.78 and 182.68 Ma, marine biodiversity remained at a low level (Fig. 2), dominated by hypoxia-tolerant organisms like *Dacryomya ovum*, with primary producers shifting from calcareous nannoplankton and dinoflagellates to *prasinophyte* green algae (40). Episodic methane emissions to the atmosphere generated discrete thermal perturbations, while concurrent methane flux across the water column may have progressively depleted dissolved oxygen reserves (64). Although the spatial development of ocean anoxia was significantly limited compared to globally distributed records of negative carbon isotope excursions (65), the transient hyperthermal conditions and expanding water column deoxygenation may have jointly driven a sustained biotic crisis throughout the T-OAE. The ecosystem only began to recover gradually once methane emissions ceased and the climate stabilized at ~182.704 Ma.

A significant release of methane likely caused pCH_4 to rise from a steady state of 0.8 ppm to a peak of ~15 ppm during T-OAE (Fig. 2*E*), with a rise rate between 0.03 to 0.34 ppm y^{-1} (*SI Appendix*, Table S7). The mean pCH_4 rise rate is close to the post–Industrial Revolution anthropogenic rate (~ 0.1 ppm y^{-1}) (66), but the upper bound far exceeds it. Although the total carbon emission rate during the T-OAE (≤1.3 Gt C y^{-1})) was lower than the modern fossil fuel consumption rate (~10 Gt C y^{-1}) (67), pCH_4 rise rates (~0.03 to 0.34 ppm y^{-1}, *SI Appendix*, Table S7) were comparable to or even exceeded current levels (~0.05 ppm y^{-1}) (66). This suggests that rapid, pulsed methane releases could be triggered once certain environmental thresholds are exceeded, offering key insights for future projections.

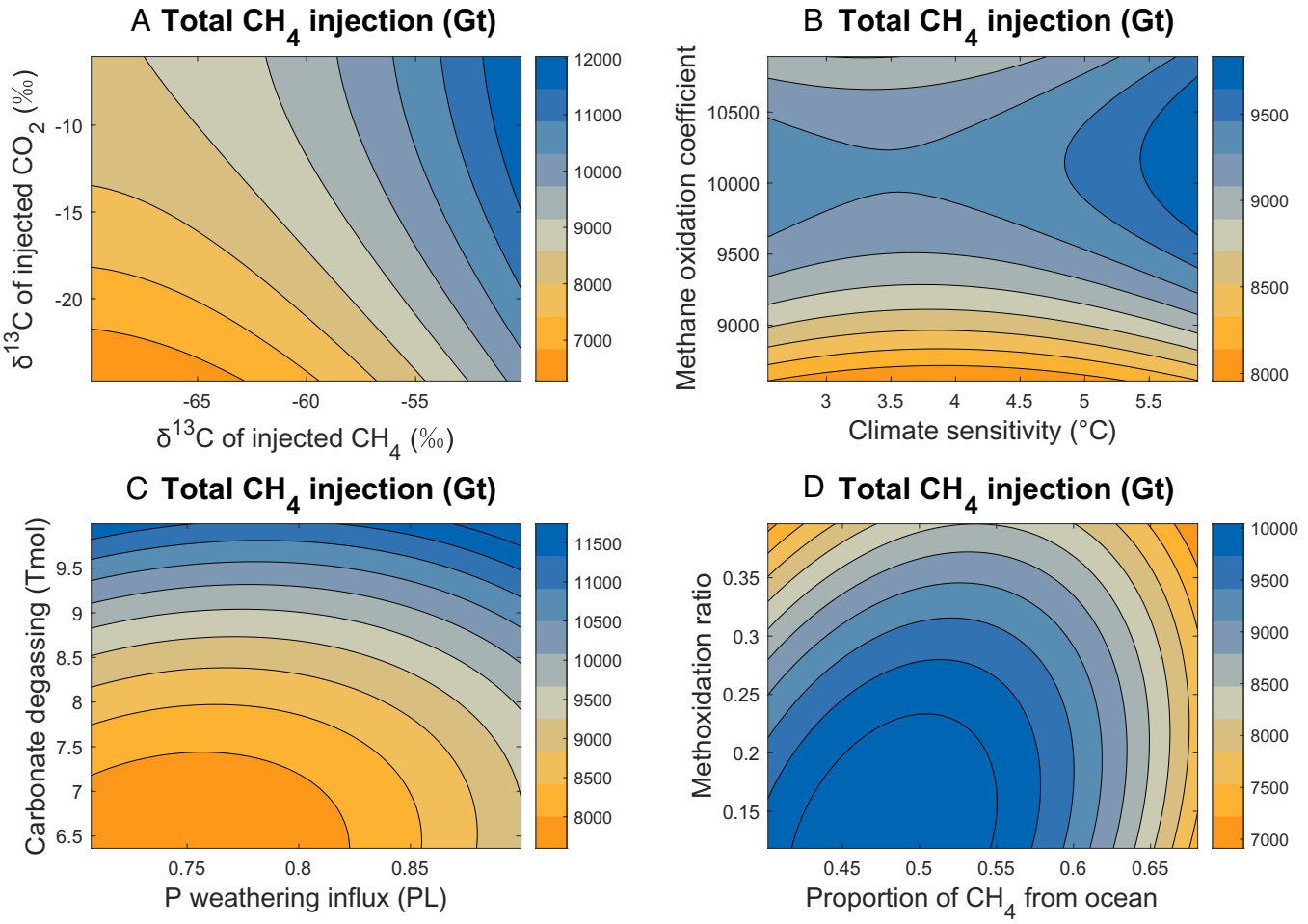

Fig. 4. Required range of CH_4 injection revealed by the CHEES model. The marine methane reservoir was included in these simulations. (*A*) Effects of $\delta^{13}C$ values of injected methane ($\delta^{13}C_{CH4}$) and $\delta^{13}C$ of injected CO_2 ($\delta^{13}C_{CO2}$). (*B*) Influence of long-term climate sensitivity (k_{clim}) and methane oxidation coefficient (km). (*C*) Impact of carbonate degassing and phosphorus weathering fluxes. (*D*) Effects of the proportion of methane oxidized in the water column and the proportion of methane release from the ocean. Lower $\delta^{13}C_{CO2}$ values, combined with lower $\delta^{13}C_{CH4}$ values, lead to reduced total CH_4 injection. When $\delta^{13}C_{CH4}$ and $\delta^{13}C_{CO2}$ take their most negative values within the specified ranges ($\delta^{13}C_{CH4}$ at −70‰ and at $\delta^{13}C_{CO2}$ −25‰), the minimum total CH_4 injection is obtained (>5,200 Gt C) (*SI Appendix*, Fig. S20). This value corresponds to model runs assuming constant isotope fractionation between atmospheric CO_2 and recording substrates. Additional sensitivity simulations incorporating a CO_2-dependent isotope fractionation mechanism yield a slightly lower requirement of ~4,700 Gt C from methane, as detailed in *SI Appendix* Figs. S24–S26.

We conclude that the widespread release of biogenic methane from a dynamic methane capacitor system, sustained by benthic microbial methanogenesis, played a crucial role in driving the negative $\delta^{13}C$ excursions and rapid warming during the Toarcian period. Once methane release is initiated, it forms a positive feedback loop with warming, making Earth more vulnerable to catastrophic climate imbalances and biological crises. The ongoing anthropogenic climate warming has the potential to trigger more vigorous methane cycling, with substantial climatic and ecosystem consequences.

Materials and Methods

Model Description. The CHemical Evolution of Earth Surface spheres (CHEES) model, which builds on ref. 28, is a box model designed to simulate C–O–S–P–Fe cycling among the oceanic, atmospheric, and sedimentary reservoirs over timescales ranging from centuries to millions of years. The model contains five ocean boxes: margin (sm), deep margin (dm), surface (s), high-latitude surface (h), and deep (d). All the surface ocean boxes are coupled to a single box atmospheric. The transport of fluxes between boxes is represented in the model, as illustrated by arrows in *SI Appendix*, Fig. S2. Compared to the reactions in ref. 28, we have also included methane oxidation in the water column and the atmosphere. Our aim here was to establish a model that links key biogeochemical processes triggered by methane plume eruptions and to estimate the potential variability in past atmospheric methane concentrations. This modeling effort focused on the variation in the residence time of methane with changes in atmospheric oxygen levels and methane production, as well as the impact of pCH_4 on global warming. Specifically, we incorporated several modifications into the fundamental structure of the model: 1) the mass balance equation of CH_4 is added; 2) the generation of methane in sediments and oxidation in the water column is supplemented; 3) the reaction between CH_4 and O_2 in the atmosphere is considered; 4) the contribution of changes in pCH_4 to temperature change is quantified; 5) the model is encapsulated and run externally using the MCMC approach for inversion (*SI Appendix*, Fig. S1). Model species, fluxes, equations, and present values are provided in the *SI Appendix*, Tables S1–S3.

Carbon Isotope Mass Balance. The model considers inputs of both CH_4 and CO_2 (derived from the solid Earth) into the ocean and atmosphere system. Input fluxes of CO_2 include direct volcanic degassing and organic carbon oxidation, with a carbon isotopic composition in the range of −5‰ (68) to −25‰ (69–71) to reflect the lower isotopic values characteristic of organic carbon and the higher values typical of mantle-derived carbon. The combined fluxes of CH_4 and CO_2 determine the initial $\delta^{13}C$ value of total carbon input into the ocean–atmosphere system and are described as follows.

$$C_{input} = f_{CH_4} + f_{vc}, \quad [1]$$

$$\delta^{13}C_{total} \times (f_{CH_4} + f_{vc}) = \delta^{13}C_{CH_4} \times f_{CH_4} + \delta^{13}C_{vc} \times f_{vc}. \quad [2]$$

Here, f_{CH4} and f_{vc} are the fluxes of CH_4 and CO_2 released, respectively, while C_{input} is the total released flux. $\delta^{13}C_{total}$ is the carbon isotopic value of the total carbon input. $\delta^{13}C_{CH4}$ and $\delta^{13}C_{vc}$ are the carbon isotopic values of released CH_4 and CO_2, respectively. Combining Eqs. **1** and **2** yields:

$$f_{vc} = (C_{input} \times \delta^{13}C_{total} + abs(\delta^{13}C_{CH4}) \times C_{input})/(abs(\delta^{13}C_{CH4}) + \delta^{13}C_{vc}), \quad [3]$$

$$f_{CH4} = C_{input} - (C_{input} \times \delta^{13}C_{total} + abs(\delta^{13}C_{CH4}) \times C_{input})/(abs(\delta^{13}C_{CH4}) + \delta^{13}C_{vc}). \quad [4]$$

Oxidation of Methane. Methane is assumed to be generated in bottom sediments and subsequently undergoes oxidation in the water column. The portion that escapes oxidation is eventually released into the atmosphere. Methane is oxidized through its reaction with oxygen, represented by the following equation:

$$CH_4 + 2O_2 \rightarrow CO_2 + 2H_2O, \quad [5]$$

where 1 mol of methane is oxidized by 2 moles of oxygen to form 1 mol of CO_2 and 2 moles of H_2O.

The benthic fluxes of methanogenesis are calculated using

$$f_{beniCH4_i} = 0.5 * (Sed_i - f_{mocb_i})/r_{CO} \cdot \frac{\frac{C_{SO4_i}}{C_{SO40_i}} \cdot f_{anR} \cdot \frac{K_{SO4}}{C_{SO4_i} + K_{SO4}}}{\frac{C_{O2_i}}{C_{O20_i}} \cdot (1 - f_{anR}) + \frac{C_{SO4_i}}{C_{SO40_i}} \cdot f_{anR}}. \quad [6]$$

Here, K_{SO4} is the Monod constant of SO_4 for respiration; r_{CO} is the C:O ratio for organic carbon respiration; C_{SO4_i} is the sulfate concentration of the ocean box that is in contact with sediments; C_{O20_i} and C_{SO40_i} are modern oxygen and sulfate concentrations in the ocean box; and f_{anR} is the proportion of anaerobic respiration in marine sediments.

Due to the setup of our model structure (*SI Appendix*, Fig. S2), methane originating from the shallow-margin sediments is sequentially consumed in the shallow margin box and the atmosphere. Methane from the deep margin sediments is first consumed in the deep margin box and then in the shallow margin box. Similarly, Methane from the deep ocean sediments is consumed in sequence by the deep, surface, and high-latitude ocean boxes. A Monod scheme is employed to describe the sequential consumption of methane across ocean boxes. Therefore, the oxidation rate of methane from marine sediments in ocean boxes (f_{CH4O_i}) and in the atmosphere (f_{CH4O_A}) is calculated as follows:

$$f_{CH4O_{sm}} = f_{beniCH4_{sm}} \cdot \frac{C_{O2_{sm}}}{C_{O20_{sm}} + K_{O2m}} + f_{beniCH4_{dm}} \cdot \frac{K_{O2m}}{C_{O20_{dm}} + K_{O2m}}, \quad [7]$$

$$f_{CH4O_{dm}} = f_{beniCH4_{dm}} \cdot \frac{C_{O2_{dm}}}{C_{O20_{dm}} + K_{O2m}}, \quad [8]$$

$$f_{CH4O_d} = f_{beniCH4_d} \cdot \frac{C_{O2_d}}{C_{O20_d} + K_{O2m}}, \quad [9]$$

$$f_{CH4O_s} = f_s \cdot f_{beniCH4_d} \cdot \frac{K_{O2m}}{C_{O20_d} + K_{O2m}}, \quad [10]$$

$$f_{CH4O_h} = (1 - f_s) \cdot f_{beniCH4_d} \cdot \frac{K_{O2m}}{C_{O20_d} + K_{O2m}}, \quad [11]$$

$$f_{CH4O_A} = f_{beniCH4_p} \cdot \frac{K_{O2m}}{C_{O20_p} + K_{O2m}}, \quad [12]$$

where K_{O2m} is the limiting concentration of oxygen for methanogenesis, f_s is the ratio of the area of surface ocean relative to the sum of the areas of the surface ocean and the high-latitude ocean.

The differential equation for the methane concentration in the atmosphere at time t is as follows:

$$\frac{dCH_{4a}}{dt} = f_{CH40} + f_{CH4} - f_{CH_4om}. \quad [13]$$

Here, f_{CH4om} represents the initial background flux at steady state, including total emissions from both terrestrial and marine sediments. GCM simulations indicate that a flux of 10 Tmol y^{-1} (approximately 0.12 Gt C y^{-1}) can maintain atmospheric methane concentrations at ~0.8 ppm (72). We assume that prior to both the Industrial Revolution and the T-OAE, in the absence of additional methane emissions, the system was in steady state (66), with atmospheric methane sustained primarily by natural sources. Accordingly, we set f_{CH40} 10 Tmol y^{-1}. At time t, the change in the reservoir of atmospheric methane equals total CH_4 emission minus the methane oxidation rate. The total methane emissions include both the steady-state flux and the additional emissions induced by climate perturbations during the T-OAE. Additionally, the flux of CO_2 generated by methane oxidation is incorporated into the mass balance equation for atmospheric CO_2 concentration.

The mass balance equation for the CO_2 concentration in the atmosphere at time t is:

$$\frac{dCO_2}{dt} = -f_{airseap} - f_{airseas} - f_{airseah} + f_{ccdeg} + f_{ocdeg} + f_{oxidw} - f_{locb} - f_{carbw} - 2f_{silw} + f_{CH_4}om + f_{vc} - f_{CH40}, \quad [14]$$

where f_{airsea_i} is the exchange of C between box i and atmosphere, f_{ccdeg} is the flux of volcanic degassing, f_{ocdeg} is the flux of organic carbon degassing, and f_{silw} and f_{carbw} are the weathering fluxes of silicate and carbonates, respectively.

During the Early Jurassic, methane residence times may have been longer than at present because 1) potentially lower atmospheric oxygen levels (73), which limited OH radical production via ozone photolysis and thus slowed methane oxidation in both the troposphere and stratosphere; and 2) a substantial increase in methane flux that could have saturated atmospheric oxidation sinks, further prolonging its residence time. Methane oxidation in the atmosphere can be approximated as a first-order decay process, with the rate dependent on atmospheric OH and Oâ„¢ concentrations. A nonlinear formulation that incorporates atmospheric oxidants describes methane oxidation and is given by the following equation (29).

$$f_{CH_4om} = km \times O_2^x \times M^{kx}. \quad [15]$$

Here, f_{CH4om} is the flux of methane oxidized to CO_2. *km* is a constant. The *kx* is the reaction order with respect to atmospheric methane concentration, and we used 0.65 as the value for *kx* based on ref. 72. Changes in atmospheric oxygen concentration (pO_2) were incorporated into the equation, and based on present-day and Precambrian oxygen levels and residence times (29), the exponent *x* was estimated to be 1.83. The constant *km* was constrained based on the modern methane residence time (8 to 12 y), yielding a range of 8.5×10^3 to 11×10^3. An initial methane eruption flux was imposed to determine the steady-state atmospheric methane concentration. The atmospheric residence time was then calculated by dividing the total methane mass by the sum of the eruption flux and the steady-state oxidation rate.

Effect of Methane on Temperature. The portion of methane that reaches the atmosphere is a potent greenhouse gas with a 100-year global warming potential ~23 times that of carbon dioxide (74). Therefore, it is critical to consider the effect of changes in methane fluxes on climate. We ran a one-dimensional photochemical and radiative climate model (75, 76), using different CH_4 concentrations as inputs, and retrieved near-surface temperatures from the vertical atmospheric profile (*SI Appendix*, Table S4). The results showed changes in surface temperature across varying methane concentrations (*SI Appendix*, Fig. S3). The empirical equation derived from the fitting was subsequently integrated into our CHEES model to estimate the global average surface temperature (GAST), as follows (70):

$$GAST = 288 + k_{clim}\left(\frac{\log\left(\frac{CO_2 ppm}{280}\right)}{\log(2)}\right) + \left(4.361 \times CH_4 ppm^{0.1467} - 4.0461\right) - 7.4\left(\frac{t_{geol}}{-570}\right), \quad [16]$$

where k_{clim} is the long-term climate sensitivity, CO_2ppm and CH_4ppm are the atmospheric concentration of CO_2 and CH_4 respectively, and t_{geol} represents time in millions of years before the present and is expressed as a negative value.

Atmospheric CO_2 and methane volume ratios (in ppm) are calculated as:

$$CO_2 ppm = 280\frac{CO_{2a}}{CO_{2a_0}}, \quad [17]$$

$$CH_4 ppm = 0.8\frac{CH_{4a}}{CH_{4a_0}}, \quad [18]$$

where CO_{2a} and CH_{4a} are atmospheric CO_2 and CH_4 in moles, CO_{2a0} and CH_{4a0} are the values at present day (pre–Industrial Revolution).

MCMC Inversion Methodology. This study introduces a time-sequential progression Bayesian inversion method based on the Metropolis algorithm within the MCMC sampling framework. This method combines robust global optimization capabilities, adaptability to complex models, insensitivity to initial values, clear probabilistic interpretations, and dynamic adjustment mechanisms, while also capturing detailed high-frequency transformations. Our inversion methodology encompasses six modules (*SI Appendix*, Fig. S1): sensitivity analysis, parameter update, parameter proposal, model execution, likelihood calculation, and adaptation.

The initialization of model parameters is categorized into three main groups: control parameters for the inversion process (control parameter), system parameters for model operation (system parameter), and parameters related to carbon release (emission parameter). The system parameters include the range of climate sensitivity, methane oxidation coefficient, carbonate degassing flux, and phosphorus weathering flux. These three parameters, once input by the external sensitivity analysis module, remain unchanged during the internal cycles. Multiple sets of system parameters are stochastically generated externally to evaluate the model's sensitivity. Control parameters, which regulate the inversion process, are continuously adjusted based on the iteration state to ensure efficient iterations and effective parameter space exploration. Emission parameters are the key parameters to be inverted in this study. There are three main parameters: CO_2 release, CH_4 release, and $\delta^{13}C$ of the released CH_4 (*SI Appendix*, Table S5). The initial values of these parameters are shown in *SI Appendix*, Tables S1–S3 and S5.

These initial parameters create a set of inputs φ_0 for the model execution module, which returns outputs of $\delta^{13}C$, atmospheric CO_2 and temperature. A stepwise perturbation in position and amplitude is applied to the initial inputs φ_0 to generate a series of input sets, φ_1 to φ_N in the parameter proposal module. Next, the input sets φ_1 to φ_N are passed to the model execution module for parallel processing, which obtains the corresponding results for each input set. We then compute the total log-likelihood for the given proposal, which is based on the degree of match between the model outputs and the observed values, using the following formula:

$$ll = ll\_\delta^{13}C + ll\_pCO_2 + ll\_SST, \quad [19]$$

$$ll\_\delta^{13}C = logpdf\left(Normal\left(\delta^{13}C_{observed}, \delta^{13}C_{std}\right), \delta^{13}C_{model}\right), \quad [20]$$

$$ll\_pCO_2 = \max\left(0, \min\left(pCO_{2_{observed}} - pCO_{2_{model}}, pCO_{2_{model}} - pCO_{2_{observed}}\right)\right), \quad [21]$$

$$ll\_SST = \max\left(0, \min\left(SST_{observed} - GAST_{model}, GAST_{model} - SST_{observed}\right)\right). \quad [22]$$

Here, the total log-likelihood (ll) calculation requires three inputs: the mean and SD of observational data, as well as values output from the model, which comprises the log-likelihood from $\delta^{13}C$ (ll_$\delta^{13}C$), atmospheric CO_2 (ll_pCO_2), and temperature (ll_SST). For $\delta^{13}C$, the normal log-likelihood is calculated progressively and used to compare iterations when accepting new proposals. For temperature and CO_2, if the simulated values lie within the CI of observational data, their log-likelihood is assigned as zero. If they fall outside this interval, we compute their deviation from the mean value, assigning a negative log-likelihood accordingly. This method accurately replicates rapid minor fluctuations in the $\delta^{13}C$ curve during the negative excursion process.

Once the initial carbon inputs φ_0 yield the first total log-likelihood ll_0 upon computation, subsequent candidate input sets φ_1 to φ_N generate a new set of log-likelihoods ll_1 to ll_N. If $ll_0 < ll_i$, then φ_0 is updated to the new proposal φ_i, where ll_i represents the maximum value among new log-likelihoods. Conversely, a new proposal is accepted with a probability equal to the ratio of the likelihoods based on the Metropolis algorithm.

Our adaptation module dynamically adjusts parameter generation and search strategies during iterations to enhance algorithm efficiency and convergence. Monitoring consecutive rejections, if new candidate parameter combinations are rejected consecutively eight times, we reduce the mean width and amplitude of perturbations by 10%. This adjustment favors smaller and narrower perturbations, increasing the likelihood of proposal acceptance (39). Additionally, as the number of iterations increases, we progressively reduce the magnitude of perturbations and time windows to adapt to changing search demands and improve the fit between simulations and target records. The initial time window is set at 50 ky, with the initial perturbation values for total release and isotopes set at 5×10^{12} mol and 10‰, respectively, as detailed in *SI Appendix*, Table S5. Although shortening time windows to increase the number of iterations extends the model runtime, it allows for more extensive exploration of high-frequency isotopic fluctuations. This allows the simulation to capture high-frequency variations while remaining aligned with the low-frequency trends of the target curve, demonstrating robust convergence regardless of initial deviations from observational data.

Experimental Scenarios and Sensitivity Analysis. We designed a total of 6 experimental scenarios (*SI Appendix*, Tables S5 and S6). In Scenarios 1 to 3, $\delta^{13}C_{CH4}$ was set to vary over time between −30 and −70‰, while $\delta^{13}C_{CO2}$ was either randomly sampled within the range of −5 to −25‰ (Scenario 1) or fixed at −25‰ (Scenario 2) and −5‰ (Scenario 3), respectively. These three scenarios allow the inversion process to dynamically determine $\delta^{13}C_{CH4}$ values required to reproduce the Toarcian paleoenvironment conditions. In Scenario 4, $\delta^{13}C_{CH4}$ was set between −30 and −40‰ to simulate methane originating entirely from thermal alteration of coal. In Scenario 5, $\delta^{13}C_{CH4}$ was set within the range of −50 to −70‰ to simulate methane entirely from biogenic sources. The injected $\delta^{13}C_{CO2}$ was randomly sampled between −5‰ and −25‰. Both $\delta^{13}C_{CH4}$ and $\delta^{13}C_{CO2}$ values were externally specified and held constant throughout each individual model simulation. Considering the impact of varying parameter configurations (climate sensitivity–k_{clim}, methane oxidation coefficient–*km*, the assumed $\delta^{13}C$ values of CH_4 and CO_2 inputs, carbonate degassing flux, and phosphorus weathering flux) on the model outputs, we assessed their sensitivity by repeatedly initializing these parameters randomly in the context of Scenario 5 and running the model to convergence. In Scenario 6, to comprehensively evaluate the environmental impacts of marine methane reservoir release, we enhanced the CHEES model by incorporating the marine methane reservoir and integrating it with the exogenous carbon cycle (*SI Appendix*, Text 5). The parameter configuration was maintained consistent with that of Scenario 5 to ensure comparability. Building upon the sensitivity analysis conducted in Scenario 5, we incorporated three additional critical parameters specifically related to the marine methane reservoir release process: 1) the diffusion coefficient of methane from sediments into the water column ($k_{CH4diff}$), 2) the oceanic contribution ratio to total methane release ($k_{oceanCH4}$), and 3) the oxidation efficiency of methane within the water column ($k_{oxiwaterCH4}$). Each scenario included multiple simulations (e.g., n = 1000). Detailed information can be found in SI *Appendix*, Table S6.

We ran the MCMC algorithm in parallel on the High-Performance Computing (HPC) platform. We randomly generated one thousand sets of system parameter conditions from the sensitivity analysis module, which were fed into the CHEES model for outer-loops simulations. The computations were distributed across 20 nodes, each handling 50 cases. Each independent case iterated 120 times, generating 448 random proposal parameters per iteration, using 64 cores for parallel processing. Results were saved after each independent iteration, with each case completing in approximately 1.5 h, for a total runtime of ~75 h.

Data, Materials, and Software Availability. All study data are included in the article and/or supporting information.

ACKNOWLEDGMENTS. We sincerely thank Gerald (Jerry) Dickens and the two anonymous reviewers for their thorough and constructive reviews. Their insightful comments prompted us to reevaluate key aspects of our interpretation, clarify methodological assumptions, and strengthen the broader context of our findings. The manuscript has benefited substantially from their thoughtful and critical input, and we are grateful for the time and expertise they dedicated to improving the quality and clarity of this work. This study was funded by the Strategy Priority Research Program (Category B) of Chinese Academy of Sciences (Grant No. XDB0710000), National Natural Science Foundation of China (grants 92255303, 42202162, and 42302339) and the IGGCAS Key program (no. IGGCAS-202201). B.J.W.M. is funded by UKRI (EP/Y008790/1 and NE/Y00650X/1).

Author affiliations: [a]Key Laboratory of Deep Petroleum Intelligent Exploration and Development, Institute of Geology and Geophysics, Chinese Academy of Sciences, Beijing 100029, China; [b]University of Chinese Academy of Sciences, Beijing 100049, China; [c]School of Earth and Environment, University of Leeds, Leeds LS2 9JT, United Kingdom; [d]Institute of Energy, Peking University, Beijing 100871, China; [e]Environmental Research Institute, University of Waikato, Tauranga 3110, New Zealand; and [f]State Key Laboratory of Lithospheric and Environmental Coevolution, Institute of Geology and Geophysics, Chinese Academy of Sciences, Beijing 100029, China

1. M. S. Storm *et al.*, Orbital pacing and secular evolution of the Early Jurassic carbon cycle. *Proc. Natl. Acad. Sci. U.S.A.* **117**, 3974–3982 (2020).
2. L. Nordt, D. Breecker, J. White, Jurassic greenhouse ice-sheet fluctuations sensitive to atmospheric CO_2 dynamics. *Nat. Geosci.* **15**, 54–59 (2021).
3. W. Ruebsam, B. Mayer, L. Schwark, Cryosphere carbon dynamics control early Toarcian global warming and sea level evolution. *Glob. Planet. Change.* **172**, 440–453 (2019).
4. A. Kunert, B. Kendall, Global ocean redox changes before and during the Toarcian Oceanic Anoxic Event. *Nat. Commun.* **14**, 815 (2023).
5. D. B. Kemp, G. Suan, A. Fantasia, S. Jin, W. Chen, Global organic carbon burial during the Toarcian oceanic anoxic event: Patterns and controls. *Earth-Sci. Rev.* **231**, 104086 (2022).
6. J. J. Gómez, C. Arias, Rapid warming and ostracods mass extinction at the Lower Toarcian (Jurassic) of central Spain. *Mar. Micropaleontol.* **74**, 119–135 (2010).
7. T. Müller *et al.*, Ocean acidification during the early Toarcian extinction event: Evidence from boron isotopes in brachiopods. *Geology* **48**, 1184–1188 (2020).
8. P. J. Harries, C. T. S. Little, The early Toarcian (Early Jurassic) and the Cenomanian-Turonian (Late Cretaceous) mass extinctions: Similarities and contrasts. *Palaeogeogr. Palaeoclimatol. Palaeoecol.* **154**, 39–66 (1999).
9. D. B. Kemp, A. L. Coe, A. S. Cohen, L. Schwark, Astronomical pacing of methane release in the early Jurassic period. *Nature* **437**, 396–399 (2005).
10. N. Thibault *et al.*, The wider context of the Lower Jurassic Toarcian oceanic anoxic event in Yorkshire coastal outcrops, UK. *Proc. Geol. Assoc.* **129**, 372–391 (2018).
11. S. P. Hesselbo *et al.*, Massive dissociation of gas hydrate during a Jurassic oceanic anoxic event. *Nature* **406**, 392–395 (2000).
12. D. B. Kemp *et al.*, The timing and duration of large-scale carbon release in the early Jurassic. *Geology* **52**, 891–895 (2024).
13. A. H. Al-Suwaidi *et al.*, New age constraints on the Lower Jurassic Pliensbachian-Toarcian boundary at Chacay Melehue (Neuquen Basin, Argentina). *Sci. Rep.* **12**, 4975 (2022).
14. D. Archer *et al.*, Atmospheric lifetime of fossil fuel carbon dioxide. *Annu. Rev. Earth. Pl. Sc.* **37**, 117–134 (2009).
15. V. A. Piedrahita *et al.*, Assessing the duration of the Paleocene–Eocene thermal maximum. *Geophys. Res. Lett.* **52**, e2024GL113117 (2025).
16. M. Hermoso *et al.*, Dynamics of a stepped carbon-isotope excursion: Ultra high-resolution study of early Toarcian environmental change. *Earth Planet. Sci. Lett.* **319–320**, 45–54 (2012).
17. W. Xu *et al.*, Evolution of the Toarcian (Early Jurassic) carbon-cycle and global climatic controls on local sedimentary processes (Cardigan Bay Basin, UK). *Earth Planet. Sci. Lett.* **484**, 396–411 (2018).
18. S. P. Hesselbo, G. Pieńkowski, Stepwise atmospheric carbon-isotope excursion during the Toarcian Oceanic Anoxic Event (Early Jurassic, Polish Basin). *Earth Planet. Sci. Lett.* **301**, 365–372 (2011).
19. X. Jin *et al.*, The Jenkyns event (early Toarcian OAE) in the Ordos Basin. North China. *Glob. Planet. Change* **193**, 103273 (2020).
20. T. R. Them II *et al.*, High-resolution carbon isotope records of the Toarcian Oceanic Anoxic Event (Early Jurassic) from North America and implications for the global drivers of the Toarcian carbon cycle. *Earth Planet. Sci. Lett.* **459**, 118–126 (2017).
21. T. H. Heimdal, Y. Godderis, M. T. Jones, H. H. Svensen, Assessing the importance of thermogenic degassing from the Karoo Large Igneous Province (LIP) in driving Toarcian carbon cycle perturbations. *Nat. Commun.* **12**, 6221 (2021).
22. D. J. Beerling, S. J. Brentnall, Numerical evaluation of mechanisms driving early Jurassic changes in global carbon cycling. *Geology* **35**, 247–250 (2007).
23. G. R. Dickens, Rethinking the global carbon cycle with a large, dynamic and microbially mediated gas hydrate capacitor. *Earth Planet. Sci. Lett.* **213**, 169–183 (2003).
24. G. R. Dickens, Down the rabbit hole: Toward appropriate discussion of methane release from gas hydrate systems during the Paleocene-Eocene thermal maximum and other past hyperthermal events. *Clim. Past.* **7**, 831–846 (2011).
25. F. A. McInerney, S. L. Wing, The paleocene-eocene thermal maximum: A perturbation of carbon cycle, climate, and biosphere with implications for the future. *Annu. Rev. Earth Planet. Sci.* **39**, 489–516 (2011).
26. B. Sell *et al.*, Evaluating the temporal link between the Karoo LIP and climatic–biologic events of the Toarcian Stage with high-precision U-Pb geochronology. *Earth Planet. Sci. Lett.* **408**, 48–56 (2014).
27. L. P. Maré, M. O. De Kock, B. Cairncross, H. Mouri, Magnetic evaluation of the palaeothermal variation across the Karoo Basin. *S. Afr. J. Geol.* **119**, 435–452 (2016).
28. M. Zhao, B. J. W. Mills, W. B. Homoky, C. L. Peacock, Oxygenation of the Earth aided by mineral–organic carbon preservation. *Nat. Geosci.* **16**, 262–267 (2023).
29. D. P. Schrag, R. A. Berner, P. F. Hoffman, G. P. Halverson, On the initiation of a snowball Earth. *Geochem. Geophys. Geosyst.* **3**, 1–21 (2002).
30. M. S. Fantle, B. D. Barnes, K. V. Lau, The role of diagenesis in shaping the geochemistry of the marine carbonate record. *Annu. Rev. Earth Planet. Sci.* **48**, 549–583 (2020).
31. P. F. Hoffman, K. G. Lamothe, Seawater-buffered diagenesis, destruction of carbon isotope excursions, and the composition of DIC in Neoproterozoic oceans. *Proc. Natl. Acad. Sci. U.S.A.* **116**, 18874–18879 (2019).
32. A. Negri, A. Ferretti, T. Wagner, P. A. Meyers, Phanerozoic organic-carbon-rich marine sediments: Overview and future research challenges. *Palaeogeogr. Palaeoclimatol. Palaeoecol.* **273**, 218–227 (2009).
33. G. Suan *et al.*, Secular environmental precursors to early Toarcian (Jurassic) extreme climate changes. *Earth Planet. Sci. Lett.* **290**, 448–458 (2010).
34. B. A. Schubert, A. H. Jahren, Incorporating the effects of photorespiration into terrestrial paleoclimate reconstruction. *Earth-Sci. Rev.* **177**, 637–642 (2018).
35. J. P. Wilson *et al.*, Dynamic carboniferous tropical forests: New views of plant function and potential for physiological forcing of climate. *New Phytol.* **215**, 1333–1353 (2017).
36. E. I. Vera, S. N. Césari, New species of conifer wood from the Baqueró Group (early Cretaceous) of Patagonia. *Ameghiniana* **52**, 468–471 (2015).
37. B. H. Lomax, C. A. Knight, J. A. Lake, An experimental evaluation of the use of C_3 $\delta^{13}C$ plant tissue as a proxy for the paleoatmospheric $\delta^{13}CO_2$ signature of air. *Geochem. Geophys. Geosyst.* **13**, 1–12 (2012).
38. C. R. Scotese, H. Song, B. J. W. Mills, D. G. Meer, Phanerozoic paleotemperatures: The Earth's changing climate during the last 540 million years. *Earth-Sci. Rev.* **215**, 103503 (2021).
39. A. A. Cox, C. B. Keller, A bayesian inversion for emissions and export productivity across the end-Cretaceous boundary. *Science* **381**, 1446–1451 (2023).
40. J. W. Atkinson, C. T. S. Little, A. M. Dunhill, Long duration of benthic ecological recovery from the early Toarcian (Early Jurassic) mass extinction event in the Cleveland Basin, UK. *J. Geol. Soc.* **180**, jgs2022-126 (2023).
41. L. M. E. Percival *et al.*, Globally enhanced mercury deposition during the end-Pliensbachian extinction and Toarcian OAE: A link to the Karoo–Ferrar Large Igneous Province. *Earth Planet. Sci. Lett.* **428**, 267–280 (2015).
42. G. R. Dickens, The potential volume of oceanic methane hydrates with variable external conditions. *Org. Geochem.* **32**, 1179–1193 (2001).
43. P. Friedlingstein *et al.*, Global carbon budget 2023. *Earth Syst. Sci. Data* **15**, 5301–5369 (2023).
44. B. Honisch *et al.*, Toward a cenozoic history of atmospheric CO_2. *Science* **382**, eadi5177 (2023).
45. L. Guo *et al.*, Acceleration of phosphorus weathering under warm climates. *Sci. Adv.* **10**, eadm7773 (2024).
46. M. Saunois *et al.*, The global methane budget 2000–2017. *Earth Syst. Sci. Data* **12**, 1561–1623 (2020).
47. T. Weber, N. A. Wiseman, A. Kock, Global ocean methane emissions dominated by shallow coastal waters. *Nat. Commun.* **10**, 4584 (2019).
48. M. Egger, N. Riedinger, J. M. Mogollón, B. B. Jørgensen, Global diffusive fluxes of methane in marine sediments. *Nat. Geosci.* **11**, 421–425 (2018).
49. A. V. Turchyn, D. J. DePaolo, Seawater chemistry through Phanerozoic time. *Annu. Rev. Earth Planet. Sci.* **47**, 197–224 (2019).
50. T. K. Lowenstein, L. A. Hardie, M. N. Timofeeff, R. V. Demicco, Secular variation in seawater chemistry and the origin of calcium chloride basinal brines. *Geology* **31**, 857–860 (2003).
51. M. Zhao, S. Zhang, L. G. Tarhan, C. T. Reinhard, N. Planavsky, The role of calcium in regulating marine phosphorus burial and atmospheric oxygenation. *Nat. Commun.* **11**, 2232 (2020).
52. L. G. Tarhan, M. Zhao, N. J. Planavsky, Bioturbation feedbacks on the phosphorus cycle. *Earth Planet. Sci. Lett.* **566**, 116961 (2021).
53. L. L. Lapham *et al.*, Methane leakage through the sulfate–methane transition zone of the Baltic seabed. *Nat. Geosci.* **17**, 1277–1283 (2024).
54. H. Sakor, S. Chiba, Dynamic programming algorithm optimization for spoken word recognition. *IEEE Trans. Acoust. Speech Signal Process.* **26**, 43–49 (1978).
55. C. C. Hay, J. R. Creveling, C. J. Hagen, A. C. Maloof, P. Huybers, A library of early Cambrian chemostratigraphic correlations from a reproducible algorithm. *Geology* **47**, 457–460 (2019).
56. C. J. Hagen, B. T. Reilly, J. S. Stoner, J. R. Creveling, Dynamic time warping of palaeomagnetic secular variation data. *Geophys. J. Int.* **221**, 706–721 (2020).
57. Y. Burstyn, A. Gazit, O. Dvir, Hierarchical dynamic time warping methodology for aggregating multiple geological time series. *Comput. Geosci.* **150**, 104704 (2021).
58. Y. Huang, X. Jin, R. D. Pancost, D. B. Kemp, B. D. A. Naafs, An intensified lacustrine methane cycle during the Toarcian OAE (Jenkyns event) in the Ordos Basin, northern China. *Earth Planet. Sci. Lett.* **639**, 118766 (2024).
59. K. M. Walter, S. A. Zimov, J. P. Chanton, D. Verbyla, F. S. Chapin, Methane bubbling from Siberian thaw lakes as a positive feedback to climate warming. *Nature* **443**, 71–75 (2006).
60. P. O. Hopcroft, P. J. Valdes, D. J. Beerling, Simulating idealized Dansgaard-Oeschger events and their potential impacts on the global methane cycle. *Quat. Sci. Rev.* **30**, 3258–3268 (2011).
61. B. Ringeval *et al.*, Response of methane emissions from wetlands to the Last Glacial Maximum and an idealized Dansgaard-Oeschger climate event: Insights from two models of different complexity. *Clim. Past.* **9**, 149–171 (2013).
62. A. L. Handwerger, A. W. Rempel, R. M. Skarbek, Submarine landslides triggered by destabilization of high-saturation hydrate anomalies. *Geochem. Geophys. Geosyst.* **18**, 2429–2445 (2017).
63. J. Geersen *et al.*, Fault zone controlled seafloor methane seepage in the rupture area of the 2010 Maule earthquake, Central Chile. *Geochem. Geophys. Geosyst.* **17**, 4802–4813 (2016).

64. M. J. Nicolo, G. R. Dickens, C. J. Hollis, South Pacific intermediate water oxygen depletion at the onset of the Paleocene-Eocene thermal maximum as depicted in New Zealand margin sections. *Paleoceanography* **25**, PA4210 (2010).
65. M. N. Remírez, T. J. Algeo, Carbon-cycle changes during the Toarcian (Early Jurassic) and implications for regional versus global drivers of the Toarcian oceanic anoxic event. *Earth-Sci. Rev.* **209**, 103283 (2020).
66. M. Rubino *et al.*, Revised records of atmospheric trace gases CO_2, CH_4, N_2O, and $\delta^{13}C$-CO_2 over the last 2000 years from Law Dome, Antarctica. *Earth Syst. Sci. Data* **11**, 473–492 (2019).
67. P. Friedlingstein *et al.*, Global carbon budget 2020. *Earth Syst. Sci. Data* **12**, 3269–3340 (2020).
68. E. Gales, B. Black, L. T. Elkins-Tanton, Carbonatites as a record of the carbon isotope composition of large igneous province outgassing. *Earth Planet. Sci. Lett.* **535**, 116076 (2020).
69. H. Jurikova *et al.*, Permian–Triassic mass extinction pulses driven by major marine carbon cycle perturbations. *Nat. Geosci.* **13**, 745–750 (2020).
70. J. Dal Corso *et al.*, Permo-Triassic boundary carbon and mercury cycling linked to terrestrial ecosystem collapse. *Nat. Commun.* **11**, 2962 (2020).
71. H. Svensen *et al.*, Siberian gas venting and the end-Permian environmental crisis. *Earth Planet. Sci. Lett.* **277**, 490–500 (2009).
72. G. A. Schmidt, D. T. Shindell, Atmospheric composition, radiative forcing, and climate change as a consequence of a massive methane release from gas hydrates. *Paleoceanography* **18**, 1–9 (2003).
73. S. J. Baker, S. P. Hesselbo, T. M. Lenton, L. V. Duarte, C. M. Belcher, Charcoal evidence that rising atmospheric oxygen terminated Early Jurassic ocean anoxia. *Nat. Commun.* **8**, 15018 (2017).
74. O. P. Karthikeyan, K. Chidambarampadmavathy, S. Cirés, K. Heimann, Review of sustainable methane mitigation and biopolymer production. *Crit. Rev. Environ. Sci. Technol.* **45**, 1579–1610 (2014).
75. A. A. Pavlov, J. F. Kasting, L. L. Brown, K. A. Rages, R. Freedman, Greenhouse warming by CH_4 in the atmosphere of early Earth. *J. Geophys. Res. Planets* **105**, 11981–11990 (2000).
76. P. Kharecha, J. Kasting, J. Siefert, A coupled atmosphere–ecosystem model of the early Archean Earth. *Geobiology* **3**, 53–76 (2005).